Physica D xxx (xxxx) xxx

Contents lists available at ScienceDirect

Physica D

journal homepage: www.elsevier.com/locate/physd

Three-dimensional map for a piecewise-linear capsule system with bidirectional drifts

Bingyong Guo, Yang Liu *

College of Engineering, Mathematics and Physical Sciences, University of Exeter, North Park Road, Exeter, EX4 4QF, UK

HIGHLIGHTS

- This paper studies a three-dimensional map for a piecewise-linear capsule system.
- The capsule system has two degrees-of-freedom involving dry friction and impact.
- Global and local dynamics of the system are studied by using the proposed map.
- All possible local mappings are obtained for a wide range of parameter variation.
- The map can be used to explain the occurrence of different bifurcations.

ARTICLE INFO

Article history:
Received 21 January 2019
Received in revised form 30 March 2019
Accepted 23 April 2019
Available online xxxx
Communicated by G. Stepan

Keywords:
Vibro-impact
Non-smooth dynamical system
Bifurcation
Dry friction
Discrete mapping

ABSTRACT

A three-dimensional map is studied in this paper to provide a fundamental understanding for the vibro-impact capsule system, which is a non-autonomous two degrees-of-freedom non-smooth dynamical system consisting of soft impact and dry friction with forward and backward drifts. By using the map, one can investigate the global and local dynamics of the system and construct all possible local mappings for a wide range of parameter variation. An example study by varying the amplitude of external excitation of the system is presented. Our results show that the proposed map can effectively explain the occurrence of the boundary-intersection crossing and the sliding bifurcations observed in the system.

1. Introduction

Locomotion mechanism has been widely used in engineering and healthcare, such as oil/gas pipe inspection [1], disaster rescue [2], and medical diagnosis and treatment [3]. These devices have external moving parts, e.g., wheels, legs or paddles, which are not suitable for the applications in complex environments, e.g., in the gastrointestinal tract. On the other hand, a locomotion mechanism without any external moving parts may have many advantages in these applications. For example, the two-mass system [4] shown in Fig. 1(a), which consists of a movable mass within a shell, has simpler and more cost-effective design than the legged capsule [5]. By controlling its inner mass periodically [6], the entire system can move forward or backward when the interaction force applied on the shell exceeds its environmental resistance. Inspired by the drifting oscillator [7], a two degrees-of-freedom vibro-impact capsule system with bidirectional drifts [8], shown in Fig. 1(b), can provide effective locomotion in a confined environment. The system consists of an inner mass attached to a capsule via a spring and a damper at one end. A secondary spring is attached to the other end of the capsule to provide visco-elastic impacts when the relative displacement between the inner mass and the secondary spring is greater than or equal to their gap. As the inner mass is driven by a harmonic force, the interaction force can overcome capsule-surface resistance and drive the capsule to move forward or backward as a whole. In order to optimise its trajectory for directional control and energy saving, understanding the dynamics of such a system, e.g., prediction of bifurcation, is vital.

Our previous work on the capsule system focused on its modelling [8], motion control [9] and model verification [10]. Both numerical and experimental studies indicate the existence of optimal orbits of the capsule system to achieve the best progression or the lowest energy consumption, and a position feedback control method was developed to follow these orbits. The capsule system takes the use of non-smoothness of the system, i.e., friction and impacts, to achieve desired locomotion. To analyse its dynamics, the system can be modelled as a piecewise-linear drifting oscillator with a set of linear and smooth subsystems, whose subspaces are divided by the non-smooth boundaries induced by friction and impacts. Although local dynamics of the

* Corresponding author.
E-mail address: y.liu2@exeter.ac.uk (Y. Liu).

https://doi.org/10.1016/j.physd.2019.04.008
0167-2789/

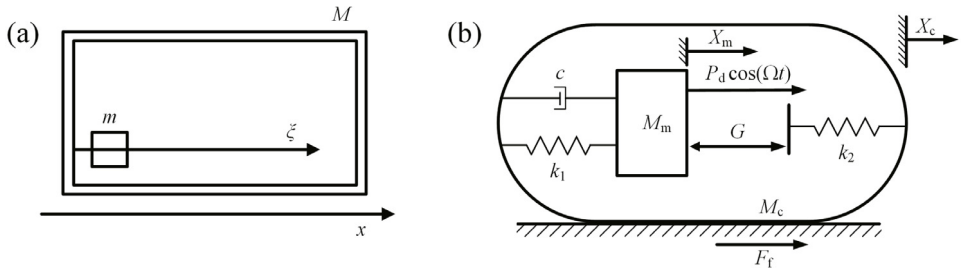

Fig. 1. Physical models of (a) the two-mass system [4], and (b) the vibro-impact capsule system with bidirectional drifts.

system has been extensively studied, e.g., [8,9,11], the root causes of bifurcation and change of locomotion direction are still not fully understood. Therefore, the global map which can interpret the switching mechanisms of the capsule dynamics across non-smooth boundaries is required. In addition, the capsule system is sensitive to its system and control parameters, e.g., the frequency and amplitude of excitation, and any parameter variation may cause a qualitative change of its dynamics. However, there is no systematic approach to study such a complex dynamics, which is the rationale of this paper.

This paper aims to study a three-dimensional (3D) map for the vibro-impact capsule system, to depict its global and local dynamics in the presence of non-smooth boundaries. Discrete mapping approaches have been widely used to investigate dynamical systems subjected to non-smoothness, e.g., [12–17]. Shaw and Holmes [12] first adopted a discrete mapping approach to study the dynamics of a periodically forced piecewise-linear oscillator. Nordmark [13] introduced local mappings between different Poincaré sections to study the grazing-induced bifurcations in an impact oscillator. Luo [14,15] proposed a mapping structure to piece together appropriate or relevant local mappings to form global mappings for a horizontal impact pair system and a ball-bouncing system. Based on Nordmark's work [13], Bernardo et al. [16] derived normal-form mappings to study sliding bifurcations. For an impact system with a drift, Pavlovskaia and Wiercigroch [17] proposed a one-dimensional analytical map to approximate a five-dimensional flow. However, these mapping approaches only consider one non-smoothness (i.e., either impacts or friction) in the system, and the impact system [17] considers the drift in one direction, while the capsule system is subjected to bidirectional drifts, friction and impacts simultaneously. Luo et al. [18] adopted a disturbed map to study the stability of periodic single-impact motions of a unidirectional plastic impact oscillator with a frictional slider. Different from Luo et al. [18], this paper aims to study the dynamics of a bidirectional visco-elastic impact system and to construct global mappings to depict the switching mechanisms between its piecewise smooth subsystems. With a special care of period-1 trajectory, Páez Chávez et al. [19] divided the trajectory of the capsule system into a smooth vector field in each disjoint subregion and studied the system by means of path-following techniques. This paper will divide the trajectory of the capsule system in the same way, but consider general periodic motions by studying all possible switching routes in the system.

The rest of this paper is organised as follows. Section 2 studies the modelling of the vibro-impact capsule system. According to the non-smoothness of the system, the 3D map is constructed in Section 3. In Section 4, case studies are provided, and the influence of the amplitude of excitation on the dynamics of the capsule system is investigated. Finally, conclusions are drawn in Section 5.

2. Modelling of the capsule system

The two degrees-of-freedom capsule system shown in Fig. 1(b) is considered in this work, where an inner mass M_m is connected to a rigid capsule M_c via a spring with stiffness k_1 and a damper with damping coefficient c. The inner mass is driven by a harmonic force $P_d\cos(\Omega t)$, where P_d, Ω and t represent the amplitude, frequency and time of the excitation, respectively. A secondary spring with stiffness k_2 is attached to the capsule and the gap between the inner mass and the secondary spring is G. X_c and V_c represent the displacement and velocity of the capsule, whilst X_m and V_m represent the displacement and velocity of the inner mass, respectively. In this study, Coulomb friction is used to calculate the frictional force between the capsule and the supporting surface,

$$\begin{cases} F_f \in [-P_f,\ P_f], & V_c = 0, \\ F_f = -\mathrm{sign}(V_c)P_f, & V_c \neq 0, \end{cases} \tag{1}$$

where $P_f = \mu(M_m+M_c)g$, μ is the friction coefficient between the capsule and the supporting surface, and g is the acceleration due to gravity. As the detailed modelling of the capsule system can be found from [8], we will study the modelling briefly as below.

When the relative displacement between the inner mass and the capsule is smaller than their gap, $X_m - X_c < G$, the secondary spring is not contacted, and hence the motion of the inner mass is governed by

$$M_m\ddot{X}_m = P_d\cos(\Omega t) - k_1(X_m - X_c) - c(\dot{X}_m - \dot{X}_c). \tag{2}$$

The dry friction between the capsule and the supporting surface may lead the capsule to move in stick–slip motion. The capsule is kept still with $\ddot{X}_c = 0, \dot{X}_c = 0$ when $|k_1(X_m - X_c) + c(\dot{X}_m - \dot{X}_c)| \leq P_f$. In this situation, the friction force can be determined by the interaction force between the inner mass and the capsule as $F_f = -k_1(X_m - X_c) - c(\dot{X}_m - \dot{X}_c)$. Also, the capsule can drift (slip) when $|k_1(X_m - X_c) + c(\dot{X}_m - \dot{X}_c)| > P_f$. So, the motion of the capsule can be expressed as

$$M_c\ddot{X}_c = F_f + k_1(X_m - X_c) + c(\dot{X}_m - \dot{X}_c), \tag{3}$$

where the friction force is determined by $F_f = -\mathrm{sign}(V_c)P_f$.

When the relative displacement is equal to or larger than the gap, $X_m - X_c \geq G$, the secondary spring is in contact, and the motion of the inner mass can be written as

$$M_m\ddot{X}_m = P_d\cos(\Omega t) - k_1(X_m - X_c) - c(\dot{X}_m - \dot{X}_c) - k_2(X_m - X_c - G). \tag{4}$$

When $|k_1(X_m - X_c) + c(\dot{X}_m - \dot{X}_c)| \leq P_f$, the capsule is kept still with $\ddot{X}_c = 0, \dot{X}_c = 0$, and the friction force can be determined by $F_f = -k_1(X_m - X_c) - c(\dot{X}_m - \dot{X}_c) - k_2(X_m - X_c - G)$. When $|k_1(X_m - X_c) + c(\dot{X}_m - \dot{X}_c) + k_2(X_m - X_c - G)| > P_f$, the capsule may drift forward or backward, governed by

$$M_c\ddot{X}_c = F_f + k_1(X_m - X_c) + c(\dot{X}_m - \dot{X}_c) + k_2(X_m - X_c - G), \tag{5}$$

where the friction force is determined by $F_f = -\mathrm{sign}(V_c)P_f$.

Please cite this article as: B. Guo and Y. Liu, Three-dimensional map for a piecewise-linear capsule system with bidirectional drifts, Physica D (2019), https://doi.org/10.1016/j.physd.2019.04.008.

Here, for simplicity, we introduce the following non-dimensional system parameters,

$$\tau = \Omega_0 t,\ \omega = \frac{\Omega}{\Omega_0},\ \alpha = \frac{P_d}{P_f},\ \zeta = \frac{c}{2M_m\Omega_0},\ \delta = \frac{k_1}{P_f}G,\ \beta = \frac{k_1}{k_2},$$
$$\gamma = \frac{M_c}{M_m},\ f_b = \frac{max(|F_f|)}{P_f},$$

to represent the non-dimensional time, excitation frequency and amplitude, damping ratio, gap, stiffness ratio, mass ratio, and friction, respectively, where $\Omega_0 = \sqrt{\frac{k_1}{M_m}}$ is the natural frequency of the capsule system. In this study, dry friction is considered, so $f_b = 1$. The non-dimensional variables of the system can be written as

$$x_c = \frac{k_1}{P_f}X_c,\ v_c = \frac{\mathrm{d}x_c}{\mathrm{d}\tau} = \frac{k_1}{\Omega_0 P_f}X_c,\ \dot{v}_c = \frac{\mathrm{d}v_c}{\mathrm{d}\tau} = \frac{k_1}{\Omega_0^2 P_f}\ddot{X}_c,$$
$$x_m = \frac{k_1}{P_f}X_m,\ v_m = \frac{\mathrm{d}x_m}{\mathrm{d}\tau} = \frac{k_1}{\Omega_0 P_f}X_m,$$

$$\dot{v}_m = \frac{\mathrm{d}v_m}{\mathrm{d}\tau} = \frac{k_1}{\Omega_0^2 P_f}\ddot{X}_m,\ x_r = x_m - x_c,\ v_r = v_m - v_c,$$

which are the non-dimensional capsule's displacement, velocity and acceleration, inner mass's displacement, velocity and acceleration, the relative displacement and velocity between the inner mass and the capsule, respectively.

Therefore, the equations of motion for the capsule system can be rewritten in a compact form as follows (cf. [8])

$$\begin{cases} \dot{x}_m &= v_m, \\ \dot{v}_m &= \alpha\cos(\omega\tau) - x_r - 2\zeta v_r - H_3\beta(x_r - \delta), \\ \dot{x}_c &= v_c, \\ \dot{v}_c &= (H_1(1-H_3) + H_2H_3)\,(-\mathrm{sign}(v_c)f_b + x_r + 2\zeta v_r \\ &\quad + H_3\beta(x_r - \delta))/\gamma, \end{cases} \tag{6}$$

with $H_1 := H(|x_r + 2\zeta v_r| - f_b)$, $H_2 := H(|x_r + 2\zeta v_r + \beta(x_r - \delta)| - f_b)$, $H_3 := H(x_r - \delta)$, where $H(\cdot)$ stands for the Heaviside step function.

We define the state space of the capsule system as $x := (x_r, v_r, v_c)$ and introduce four auxiliary functions,

$$\begin{cases} P_1(x) := v_c, \\ P_2(x) := x_r, \\ P_3(x) := x_r + 2\zeta v_r, \\ P_4(x) := x_r + 2\zeta v_r + \beta(x_r - \delta). \end{cases}$$

As the capsule system moves in a vibro-impact stick–slip manner, $P_1(x) = 0$ represents the non-smooth plane induced by dry friction, and $P_2(x) = \delta$ represents the non-smooth plane induced by impacts. On the non-smooth plane of $P_1(x) = 0$, $P_3(x) = \pm f_b$ and $P_4(x) = \pm f_b$ are the boundaries of slip regions.

Next, we divide the trajectories of the piecewise-linear model Eq. (6) by introducing the following six segments.

No contact-forward drift (NC-FD). For $x \in \Omega_1 := \{x|\, P_1(x) > 0, P_2(x) \le \delta\} \cup \{x|\, P_1(x) = 0, P_2(x) \le \delta, P_3(x) > f_b\}$, the equations of motion can be rewritten as

$$\dot{x} = F_1(x,\tau) := (v_r, -\frac{\gamma+1}{\gamma}P_3(x) + \frac{f_b}{\gamma} + \alpha\cos(\omega\tau),\ \frac{P_3(x) - f_b}{\gamma}). \tag{7}$$

No contact-stick (NC-S). For $x \in \Omega_2 := \{x|\, P_1(x) = 0, P_2(x) \le \delta, |P_3(x)| \le f_b\}$, the capsule system is governed by

$$\dot{x} = F_2(x,\tau) := (v_r, -P_3(x) + \alpha\cos(\omega\tau), 0). \tag{8}$$

No contact-backward drift (NC-BD). For $x \in \Omega_3 := \{x|\, P_1(x) < 0, P_2(x) \le \delta\} \cup \{x|\, P_1(x) = 0, P_2(x) \le \delta, P_3(x) < -f_b\}$, the equations of motion can be written as

$$\dot{x} = F_3(x,\tau) := (v_r, -\frac{\gamma+1}{\gamma}P_3(x) - \frac{f_b}{\gamma} + \alpha\cos(\omega\tau),\ \frac{P_3(x) + f_b}{\gamma}). \tag{9}$$

Contact-forward drift (C-FD). For $x \in \Omega_4 := \{x|\, P_1(x) > 0, P_2(x) \ge \delta\} \cup \{x|\, P_1(x) = 0, P_2(x) \ge \delta, P_4(x) > f_b\}$, the capsule system is governed by

$$\dot{x} = F_4(x,\tau) := (v_r, -\frac{(\gamma+1)}{\gamma}P_4(x) + \frac{f_b}{\gamma} + \alpha\cos(\omega\tau),\ \frac{P_4(x) - f_b}{\gamma}). \tag{10}$$

Contact-stick (C-S). For $x \in \Omega_5 := \{x|\, P_1(x) = 0, P_2(x) \ge \delta, |P_3(x)| \le f_b\}$, the equations of motion of the capsule system can be written as

$$\dot{x} = F_5(x,\tau) := (v_r, -P_4(x) + \alpha\cos(\omega\tau), 0). \tag{11}$$

Contact-backward drift (C-BD). For $x \in \Omega_6 := \{x|\, P_1(x) < 0, P_2(x) \ge \delta\} \cup \{x|\, P_1(x) = 0, P_2(x) \ge \delta, P_4(x) < -f_b\}$, the equations of motion can be written as

$$\dot{x} = F_6(x,\tau) := (v_r, -\frac{(\gamma+1)}{\gamma}P_4(x) - \frac{f_b}{\gamma} + \alpha\cos(\omega\tau),\ \frac{P_4(x) + f_b}{\gamma}). \tag{12}$$

3. Switching mechanisms and 3D map

3.1. Definitions of boundary surfaces and lines

According to the non-smooth conditions of the capsule system, the boundary surfaces can be defined as

$$\begin{cases} S_1 &:= \{x|\, P_1(x) = 0, P_2(x) < \delta, P_3(x) > f_b\}, \\ S_2 &:= \{x|\, P_1(x) = 0, P_2(x) < \delta, |P_3(x)| < f_b\}, \\ S_3 &:= \{x|\, P_1(x) = 0, P_2(x) < \delta, P_3(x) < -f_b\}, \\ S_4 &:= \{x|\, P_1(x) = 0, P_2(x) > \delta, P_4(x) > f_b\}, \\ S_5 &:= \{x|\, P_1(x) = 0, P_2(x) > \delta, |P_4(x)| < f_b\}, \\ S_6 &:= \{x|\, P_1(x) = 0, P_2(x) > \delta, P_4(x) < -f_b\}, \\ S_7 &:= \{x|\, P_1(x) > 0, P_2(x) = \delta, v_r > 0\}, \\ S_8 &:= \{x|\, P_1(x) > 0, P_2(x) = \delta, v_r < 0\}, \\ S_9 &:= \{x|\, P_1(x) < 0, P_2(x) = \delta, v_r > 0\}, \\ S_{10} &:= \{x|\, P_1(x) < 0, P_2(x) = \delta, v_r < 0\}. \end{cases} \tag{13}$$

It is worth noting that, the surfaces, S_i, where $i = 1, 2, \ldots, 6$, are on the plane $P_1(x) = 0$ to represent the non-smoothness induced by dry friction. Stick motion of the capsule occurs on the surfaces, S_2 and S_5. The surfaces, S_i, where $i = 7, 8, \ldots, 10$, are on the plane $P_2(x) = \delta$ to denote the non-smoothness induced by visco-elastic impacts. For example, the trajectory of the capsule system enters impact surface through S_7 or S_9, and leaves the surface from S_8 or S_{10}.

Among these boundary surfaces, we introduce the following boundary lines to describe different bifurcation events.

$$\begin{cases} L_1 &:= \{x|\, P_1(x) = 0, P_2(x) < \delta, P_3(x) = f_b\}, \\ L_2 &:= \{x|\, P_1(x) = 0, P_2(x) \le \delta, P_3(x) = -f_b\}, \\ L_3 &:= \{x|\, P_1(x) = 0, P_2(x) \ge \delta, P_4(x) = f_b\}, \\ L_4 &:= \{x|\, P_1(x) = 0, P_2(x) > \delta, P_4(x) = -f_b\}, \\ L_5 &:= \{x|\, P_1(x) = 0, P_2(x) = \delta, v_r > -\frac{\delta}{2\zeta} + \frac{f_b}{2\zeta}\}, \\ L_6 &:= \{x|\, P_1(x) = 0, P_2(x) = \delta, 0 < v_r < -\frac{\delta}{2\zeta} + \frac{f_b}{2\zeta}\}, \\ L_7 &:= \{x|\, P_1(x) = 0, P_2(x) = \delta, -\frac{\delta}{2\zeta} - \frac{f_b}{2\zeta} < v_r < 0\}, \\ L_8 &:= \{x|\, P_1(x) = 0, P_2(x) = \delta, v_r < -\frac{\delta}{2\zeta} - \frac{f_b}{2\zeta}\}, \\ L_9 &:= \{x|\, P_2(x) = \delta, v_r = 0\}. \end{cases} \tag{14}$$

According to the vector functions, F_n, the subspaces, Ω_n, where $n = 1, 2, \ldots, 6$, are divided by the non-smooth boundary surfaces, $S_{i=1,2,\ldots,10}$, and lines, $L_{j=1,2,\ldots,9}$, which are visualised in Fig. 2.

Please cite this article as: B. Guo and Y. Liu, Three-dimensional map for a piecewise-linear capsule system with bidirectional drifts, Physica D (2019), https://doi.org/10.1016/j.physd.2019.04.008.

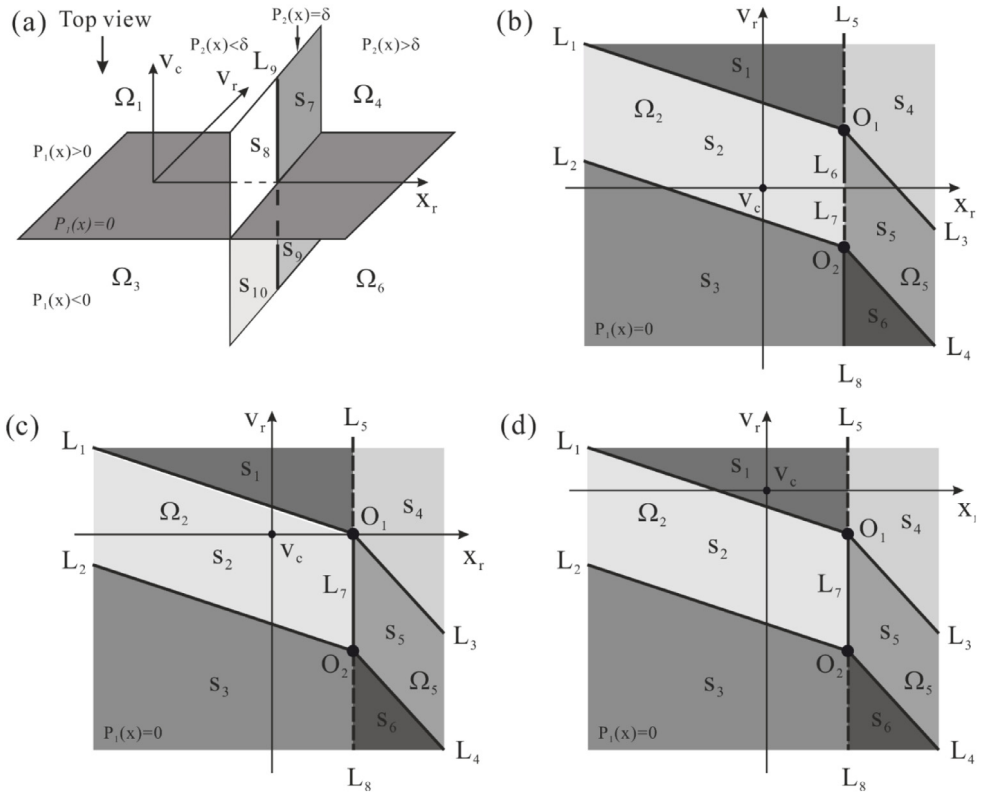

Fig. 2. (a) Subspaces, $\Omega_{n=1,2,\ldots,6}$, non-smooth boundary surfaces, $S_{i=1,2,\ldots,10}$, and lines, $L_{j=1,2,\ldots,9}$, in 3D state space. Top view of the 3D state space (i.e., the plane $P_1(x) = 0$) for (b) $\delta < f_b$, (c) $\delta = f_b$ and (d) $\delta > f_b$. The subspaces can be described as $\Omega_1 := \{x|\, P_1(x) > 0, P_2(x) \le \delta\} \cup S_1$, $\Omega_2 := S_2 \cup L_1 \cup L_2 \cup L_7$, $\Omega_3 := \{x|\, P_1(x) < 0, P_2(x) \le \delta\} \cup S_3 \cup L_8$, $\Omega_4 := \{x|\, P_1(x) > 0, P_2(x) \ge \delta\} \cup S_4 \cup L_5$, $\Omega_5 := S_5 \cup L_3 \cup L_4 \cup L_6$, and $\Omega_6 := \{x|\, P_1(x) < 0, P_2(x) \ge \delta\} \cup S_6$.

So, the subspaces can be expressed as

$$\begin{cases} \Omega_1 := \{x|\, P_1(x) > 0, P_2(x) \le \delta\} \cup S_1, \\ \Omega_2 := S_2 \cup L_1 \cup L_2 \cup L_7, \\ \Omega_3 := \{x|\, P_1(x) < 0, P_2(x) \le \delta\} \cup S_3 \cup L_8, \\ \Omega_4 := \{x|\, P_1(x) > 0, P_2(x) \ge \delta\} \cup S_4 \cup L_5, \\ \Omega_5 := S_5 \cup L_3 \cup L_4 \cup L_6, \\ \Omega_6 := \{x|\, P_1(x) < 0, P_2(x) \ge \delta\} \cup S_6. \end{cases} \tag{15}$$

As shown in Fig. 2(b), the intersection of L_1, L_3, L_5 and L_6 is $O_1 := (\delta, \frac{f_b-\delta}{2\zeta}, 0)$, and the intersection of L_2, L_4, L_7 and L_8 is $O_2 := (\delta, -\frac{f_b+\delta}{2\zeta}, 0)$, where we define $O_1 \in L_3$ and $O_2 \in L_2$ for convenience. Since $f_b \ge 0$, there are three scenarios for the location of O_1, i.e., in the top-right quarter, on the axis of x_r^+, and in the bottom-right quarter of the plane $P_1(x) = 0$ for $\delta < f_b$, $\delta = f_b$, and $\delta > f_b$, respectively. When $\delta < f_b$, if $x(0) = (0, 0, 0)$, the capsule starts from stick motion and might have drift and impact afterwards. It is noted that L_1, L_2, L_3 and L_4 are the boundary lines separating stick and drifting motions. When a trajectory hits any of these lines, sliding bifurcation may occur. L_5, L_6, L_7 and L_8 are the intersection lines of the non-smooth boundary planes $P_1(x) = 0$ and $P_2(x) = \delta$. When a trajectory hits any of these lines, boundary-intersection crossing bifurcation may occur. Furthermore, we assume that L_9 is smooth for all vector functions, $F_{n=1,2,\ldots,6}(x, \tau)$, so L_9 is not considered as a non-smooth boundary in this study. For $\delta = f_b$ and $\delta > f_b$, top views of the 3D state space in Fig. 2(a) are presented in Fig. 2(c) and (d). When $\delta = f_b$, $O_1 := (\delta, 0, 0)$ and if $x(0) = (0, 0, 0)$, the capsule will start from stick motion and must have forward drift before any impact occurs. For $\delta > f_b$, if $x(0) = (0, 0, 0)$, the capsule will start from forward drift and impact might occur afterwards. It should be noted that, for these two scenarios, $\delta = f_b$ and $\delta > f_b$, the boundary line L_6 (for contact-stick motion) doest not exist. For the location of O_2, since $-\frac{f_b+\delta}{2\zeta} < 0$, it is always in the bottom-right quarter of the plane $P_1(x) = 0$. In the following subsections, we will use the scenario, $\delta < f_b$, as an example to study the switching mechanisms in the 3D map.

3.2. Switching mechanisms on boundary surfaces

Let us define the two sides of the surface S_i as S_i^+ and S_i^-. For $i = 1, 2, \ldots, 6$, S_i^+ represents the upper half plane of S_i at where $P_1(x) \to 0^+$, and S_i^- represents its lower half plane for which $P_1(x) \to 0^-$. The normals of S_i^+ and S_i^- can be written as $\nabla P_1^+(x) = (0, 0, 1)$ and $\nabla P_1^-(x) = (0, 0, -1)$, respectively. For $i = 7, 8, 9, 10$, S_i^+ represents the right half plane of S_i at where $P_2(x) \to \delta^+$, and S_i^- represents its left half plane for which $P_2(x) \to \delta^-$, so $\nabla P_2^+(x) = (1, 0, 0)$ and $\nabla P_2^-(x) = (-1, 0, 0)$. Typical examples for the trajectories crossing S_1, S_5 and S_7 are illustrated in Fig. 3.

As shown in Fig. 3(a), a typical trajectory passes through the boundary surface S_1 via x_1^- and x_1^+. According to the definition of S_1, $P_3(x_1^-) > f_b$ and $P_3(x_1^+) > f_b$. The surface normal for S_1^- is denoted as $\nabla P_1^-(x)$, and the trajectory vector is $F_3(x, \tau)$. The surface normal for S_1^+ is denoted as $\nabla P_1^+(x)$, and the trajectory vector is $F_1(x, \tau)$. So, the approaching direction of this trajectory at x_1^- can be determined by the sign of $\langle \nabla P_1^-(x), F_3(x, \tau) \rangle$, given as

$$\left\langle \nabla P_1^-(x), F_3(x, \tau) \right\rangle\Big|_{x=x_1^-} = -\frac{P_3(x) + f_b}{\gamma}\bigg|_{x=x_1^-} < 0, \tag{16}$$

where the negative sign indicates that S_1^- is an attracting surface. The approaching direction of the trajectory at x_1^+ can be determined by the sign of $\langle \nabla P_1^+(x), F_1(x, \tau) \rangle$, given as

$$\left\langle \nabla P_1^+(x), F_1(x, \tau) \right\rangle\Big|_{x=x_1^+} = \frac{P_3(x) - f_b}{\gamma}\bigg|_{x=x_1^+} > 0, \tag{17}$$

Please cite this article as: B. Guo and Y. Liu, Three-dimensional map for a piecewise-linear capsule system with bidirectional drifts, Physica D (2019), https://doi.org/10.1016/j.physd.2019.04.008.

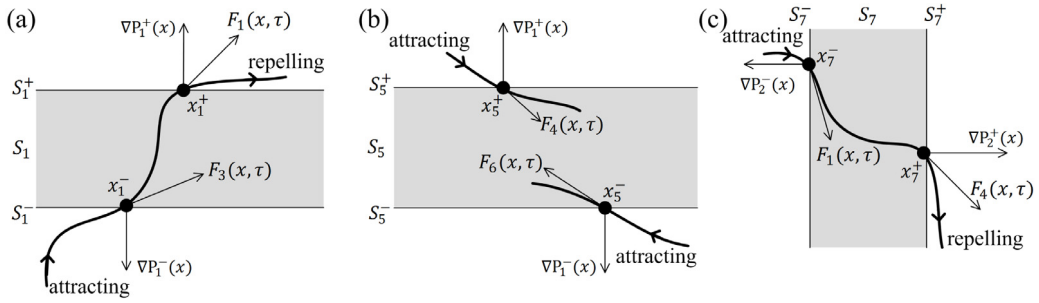

Fig. 3. Examples of the switching mechanisms for the trajectories crossing (a) S_1, (b) S_5, and (c) S_7. Bold black curves represent system trajectories and the arrows tangent to trajectories represent the corresponding vector functions. The arrows perpendicular to surfaces represent the normals of the corresponding surfaces. The switching mechanisms for the system trajectory on these non-smooth surfaces are determined by the sign of the inner product of the surface normal and the trajectory vector function. Positive and negative inner products indicate a repelling and an attracting trajectories, respectively, and zero inner product indicates trajectory grazing at boundary surface.

where the positive sign indicates that S_1^+ is a repelling surface. Therefore, the switching mechanism on the boundary surface S_1 is to attract the trajectory from Ω_3 and repel it to Ω_1. Similar switching mechanisms can be found on the boundary surfaces, S_3, S_4 and S_6, which are summarised in Table 1.

The second example of the switching mechanism is shown in Fig. 3(b), where a trajectory passes through the boundary surface S_5 by intersecting S_5^+ and S_5^- at x_5^+ and x_5^-, respectively. According to the definition of S_5 in Eq. (13), we can obtain $|P_4(x_5^+)| < f_b$ and $|P_4(x_5^-)| < f_b$. Therefore,

$$\left\langle \nabla P_1^+(x), F_4(x,\tau)\right\rangle\Big|_{x=x_5^+} = \left.\frac{P_4(x)-f_b}{\gamma}\right|_{x=x_5^+} < 0, \tag{18}$$

where $\nabla P_1^+(x)$ is the surface normal of S_5^+, $F_4(x,\tau)$ is the trajectory vector of x_5^+, and

$$\left\langle \nabla P_1^-(x), F_6(x,\tau)\right\rangle\Big|_{x=x_5^-} = \left.-\frac{P_4(x)+f_b}{\gamma}\right|_{x=x_5^-} < 0, \tag{19}$$

where $\nabla P_1^-(x)$ is the surface normal of S_5^-, and $F_6(x,\tau)$ is the trajectory vector of x_5^-. According to Eqs. (18) and (19), both S_5^+ and S_5^- are attracting surfaces, so S_5 attracts trajectory from both sides of the boundary surface. The switching mechanism on S_5 is to attract trajectory from Ω_4 and Ω_6 and repel it to Ω_5. The boundary surface S_2 has similar switching mechanism, and its switching route is given in Table 1.

For the boundary surface S_7 shown in Fig. 3(c), a trajectory intersects S_7^- and S_7^+ at x_7^- and x_7^+, respectively. We can obtain

$$\left\langle \nabla P_2^-(x), F_1(x,\tau)\right\rangle\Big|_{x=x_7^-} = -v_r < 0, \tag{20}$$

where $\nabla P_2^-(x)$ is the surface normal of S_7^-, $F_1(x,\tau)$ is the trajectory vector of x_7^-, and

$$\left\langle \nabla P_2^+(x), F_4(x,\tau)\right\rangle\Big|_{x=x_7^+} = v_r > 0, \tag{21}$$

where $\nabla P_2^+(x)$ is the surface normal of S_7^+, and $F_4(x,\tau)$ is the trajectory vector of x_7^+. According to Eqs. (20) and (21), S_7^- is an attracting surface, and S_7^+ is a repelling surface. Therefore, the switching mechanism on S_7 is to attract trajectory from Ω_1 and repel it to Ω_4. Similarly, the switching mechanisms on S_8, S_9 and S_{10}, which are summarised in Table 1, can be determined.

3.3. Switching mechanisms on boundary lines

When system trajectory hits boundary lines on the plane $P_1(x) = 0$, four types of sliding bifurcations, including adding–sliding, crossing–sliding, grazing–sliding and switching–sliding bifurcations, may occur, which are depicted in Fig. 4. As can be seen from Fig. 4(a), $\nabla P_3^+(x) = (1, 2\zeta, 0)$ is the normal of L_1 pointing from S_2 to S_1, $\nabla P_3^-(x) = (-1, -2\zeta, 0)$ is the normal of L_2 pointing from S_2 to S_3, $\nabla P_4^+(x) = (1+\beta, 2\zeta, 0)$ is the normal of L_3 pointing from S_5 to S_4, and $\nabla P_4^-(x) = (-1-\beta, -2\zeta, 0)$ is the normal of L_4 pointing from S_5 to S_6. The vector of the point x_1 on L_1 is given by $F_2(x,\tau)$, so

$$\left\langle \nabla P_3^+(x), F_2(x,\tau)\right\rangle\Big|_{x=x_1} = v_r - 2\zeta f_b + 2\zeta\alpha\cos(\omega\tau). \tag{22}$$

For $\alpha \in (0, \frac{f_b-\delta}{4\zeta^2} - f_b)$, $\left\langle \nabla P_3^+(x), F_2(x,\tau)\right\rangle\Big|_{x=x_1} > 0$, so L_1 attracts trajectories from S_2 and then repels them to S_1. The section view of L_1 is shown in Fig. 4(b), where a trajectory hits L_1 (black dot) from Ω_1, and a grazing–sliding bifurcation occurs. If a trajectory hits L_1 from Ω_3, a crossing–sliding bifurcation will occur. Therefore, the switching mechanism on L_1 is to attract trajectories from Ω_1, Ω_2 and Ω_3, and repel them to Ω_1. Similarly, the switching mechanism on L_4 is to attract trajectories from Ω_4, Ω_5 and Ω_6, and repel them to Ω_4 for $\alpha \in (0, \frac{(1+\beta)(f_b+\delta)}{4\zeta^2} - f_b)$. In this example, we assume $\alpha \in (0, \frac{f_b-\delta}{4\zeta^2} - f_b) \cap (0, \frac{(1+\beta)(f_b+\delta)}{4\zeta^2} - f_b)$, to ensure that the switching directions on L_1 and L_4 are unitary. For detailed derivations of these boundaries, one can refer to Appendix A.

For the point x_2 on the line L_2, its vector is given by $F_2(x,\tau)$, where

$$\left\langle \nabla P_3^-(x), F_2(x,\tau)\right\rangle\Big|_{x=x_2} = -v_r + 2\zeta f_b + 2\zeta\alpha\cos(\omega\tau). \tag{23}$$

Based on the amplitude of excitation α, L_2 can be divided into 3 segments as $L_2^{(1)}$ for $v_r \in [-\frac{f_b-\delta}{2\zeta}, 2\zeta f_b - 2\zeta\alpha)$, $L_2^{(2)}$ for $v_r \in [2\zeta f_b - 2\zeta\alpha, 2\zeta f_b + 2\zeta\alpha]$, and $L_2^{(3)}$ for $v_r \in (2\zeta f_b + 2\zeta\alpha, +\infty)$, which has been detailed in Appendix B. For $L_2^{(1)}$, we have $\left\langle \nabla P_3^-(x), F_2(x,\tau)\right\rangle\Big|_{x=x_2} < 0$ and system trajectories are driven out of S_2. So, the switching mechanism on $L_2^{(1)}$ is similar to that on L_1, attracting trajectories from Ω_1, Ω_2 and Ω_3, and then repelling them to Ω_3. For $L_2^{(2)}$, the sign of $\left\langle \nabla P_3^-(x), F_2(x,\tau)\right\rangle\Big|_{x=x_2}$ depends on time significantly, and consequently, adding–sliding, crossing–sliding, grazing–sliding and switching–sliding bifurcations may occur on this boundary line. The switching mechanism on $L_2^{(2)}$ is to attract trajectories from Ω_1, Ω_2 and Ω_3, and then repel them to Ω_2 or Ω_3. For $L_2^{(3)}$, we have $\left\langle \nabla P_3^-(x), F_2(x,\tau)\right\rangle\Big|_{x=x_2} > 0$, and system trajectories will approach to S_2. As shown in Fig. 4(c), when a trajectory hits $L_2^{(3)}$ from Ω_1, switching–sliding bifurcation will occur. Therefore, the switching mechanism on $L_2^{(3)}$ is to attract trajectories from Ω_1 and Ω_3, and then repel them to Ω_2.

Similarly, for a given amplitude of excitation α, L_3 can be divided into three segments as $L_3^{(1)}$ for $v_r \in (-\infty, \frac{2\zeta(f_b-\alpha)}{1+\beta})$, $L_3^{(2)}$ for $v_r \in [\frac{2\zeta(f_b-\alpha)}{1+\beta}, \frac{2\zeta(f_b+\alpha)}{1+\beta}]$, and $L_3^{(3)}$ for $v_r \in (\frac{2\zeta(f_b+\alpha)}{1+\beta}, \frac{f_b-\delta}{2\zeta}]$, which has been detailed in Appendix B. As a whole, the switching mechanism on L_3 is to attract trajectories from Ω_4, Ω_5 and Ω_6, and then

Please cite this article as: B. Guo and Y. Liu, Three-dimensional map for a piecewise-linear capsule system with bidirectional drifts, Physica D (2019), https://doi.org/10.1016/j.physd.2019.04.008.

Table 1
Switching mechanisms on the non-smooth boundary surfaces.

Surface	Source space	Target space	Source vector	Target vector	Operation mode
S_1	Ω_3	Ω_1	$F_3(x,\tau)$	$F_1(x,\tau)$	NC-BD → NC-FD
S_2	Ω_1	Ω_2	$F_1(x,\tau)$	$F_2(x,\tau)$	NC-FD → NC-S
	Ω_3	Ω_2	$F_3(x,\tau)$	$F_2(x,\tau)$	NC-BD → NC-S
S_3	Ω_1	Ω_3	$F_1(x,\tau)$	$F_3(x,\tau)$	NC-FD → NC-BD
S_4	Ω_6	Ω_4	$F_6(x,\tau)$	$F_4(x,\tau)$	C-BD → C-FD
S_5	Ω_4	Ω_5	$F_4(x,\tau)$	$F_5(x,\tau)$	C-FD → C-S
	Ω_6	Ω_5	$F_6(x,\tau)$	$F_5(x,\tau)$	C-BD → C-S
S_6	Ω_4	Ω_6	$F_4(x,\tau)$	$F_6(x,\tau)$	C-FD → C-BD
S_7	Ω_1	Ω_4	$F_1(x,\tau)$	$F_4(x,\tau)$	NC-FD → C-FD
S_8	Ω_4	Ω_1	$F_4(x,\tau)$	$F_1(x,\tau)$	C-FD → NC-FD
S_9	Ω_3	Ω_6	$F_3(x,\tau)$	$F_6(x,\tau)$	NC-BD → C-BD
S_{10}	Ω_6	Ω_3	$F_6(x,\tau)$	$F_3(x,\tau)$	C-BD → NC-BD

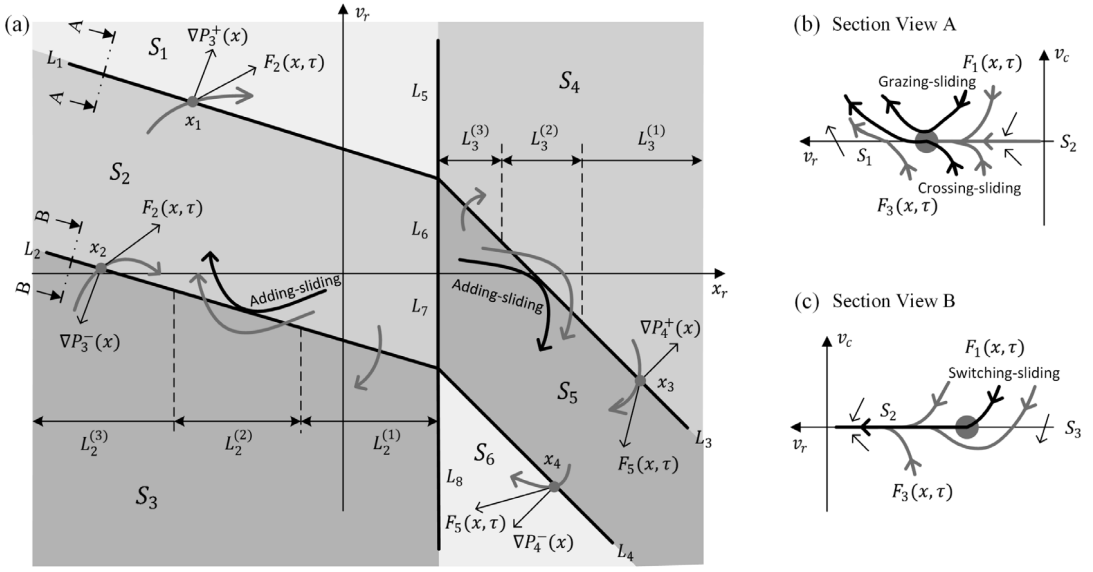

Fig. 4. (a) Switching mechanisms on boundary lines $L_{j=1,2,3,4}$, (b) section view of L_1, and (c) section view of $L_2^{(3)}$. Bold curves (grey and black) with arrows denote system trajectories, and the black ones represent the trajectories when bifurcations occur. The black arrows tangent to the trajectories denote their corresponding vector fields, and the black arrows perpendicular to $L_{j=1,2,3,4}$ represent the normals of the corresponding boundary lines.

repel them to Ω_4 or Ω_5. So, switching–sliding bifurcations can occur on $L_3^{(1)}$, all the four types of sliding bifurcations can happen on $L_3^{(2)}$, and crossing–sliding and grazing–sliding bifurcations may exist on $L_3^{(3)}$.

The switching mechanisms and possible bifurcations on the boundary lines $L_{j=5,6,7,8}$ are shown in Fig. 5, where section view of each boundary line is presented in Fig. 5(b)–(e). As can be seen from Fig. 5(b), the boundary line L_5 degenerates to a point at where the boundary-intersection crossing bifurcation will occur when system trajectory hits L_5. The switching mechanism for L_5 is to attract trajectories from Ω_3 and then repel them to Ω_4. Similarly, as shown in Fig. 5(e), the passage of L_8 indicates the occurrence of a boundary-intersection crossing bifurcation from Ω_4 to Ω_3. As can be seen from Fig. 5(c), when trajectories hit L_6 from Ω_1 and Ω_3, boundary-intersection crossing bifurcations will occur, and both trajectories enter S_5. Therefore, the switching mechanism on L_6 is to attract trajectories from Ω_1, Ω_2 and Ω_3, and then repel them to Ω_5. Opposite to L_6, as shown in Fig. 5(d), the switching mechanism on L_7 is to attract trajectories from Ω_4, Ω_5 and Ω_6, and then repel them to Ω_2.

Finally, the switching mechanisms on $L_{j=1,2,\ldots,8}$ are summarised in Table 2. It is worth noting that the boundary line L_9 satisfies the condition of grazing bifurcations. However, we have defined the vector functions $F_{n=1,2,\ldots,6}$ are smooth on L_9. It is therefore that L_9 will not be considered as a non-smooth boundary in this study.

3.4. 3D map

Based on the switching mechanisms on the boundary surfaces and lines, we can define the following switching planes for the 3D map.

$$\begin{cases} \Sigma_1 := S_1, \\ \Sigma_2 := S_2 \cup L_1 \cup L_2 \cup L_7, \\ \Sigma_3 := S_3 \cup L_8, \\ \Sigma_4 := S_4 \cup L_5, \\ \Sigma_5 := S_5 \cup L_3 \cup L_4 \cup L_6, \\ \Sigma_6 := S_6, \\ \Sigma_7 := S_7, \\ \Sigma_8 := S_8, \\ \Sigma_9 := S_9, \\ \Sigma_{10} := S_{10}. \end{cases} \tag{24}$$

According to these switching planes, local mapping, $P : \Sigma_k \to \Sigma_i$ given by $F_n(x,\tau)$, can be written as $P_{\Sigma_i,F_n,\Sigma_k}$, where $\Sigma_{i=1,2,\ldots,10}$, $F_{n=1,2,\ldots,6}$ and $\Sigma_{k=1,2,\ldots,10}$ represent the target switching plane, the vector function, and the source switching plane, respectively. In

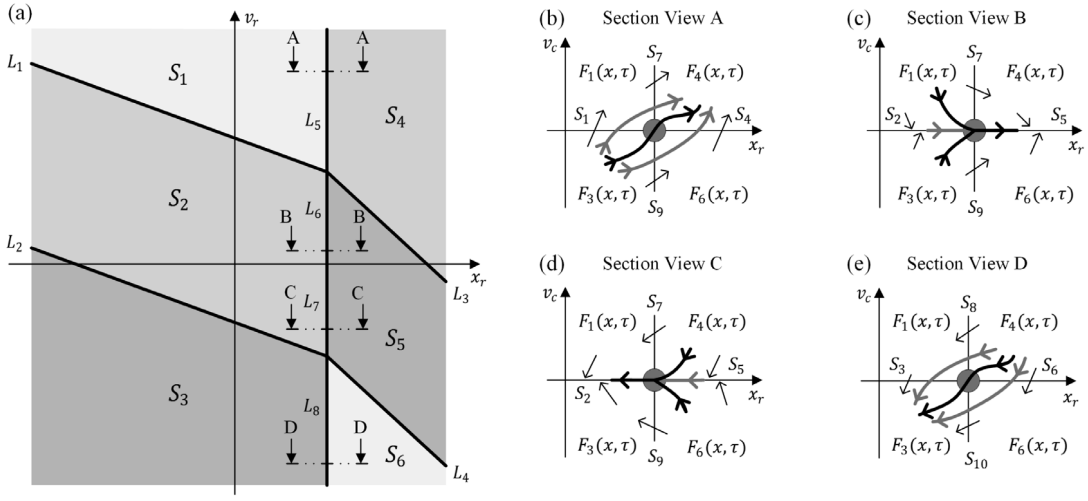

Fig. 5. (a) Switching mechanisms on boundary lines $L_{j=5,6,7,8}$, and (b)–(e) section views of $L_{j=5,6,7,8}$. Bold curves (grey and black) with arrows denote system trajectories, and the black ones represent the trajectories when bifurcations occur.

Table 2
Switching mechanisms on the non-smooth boundary lines.

Lines	Source spaces	Target spaces	Source vectors	Target vectors	Operation mode
L_1	Ω_1	Ω_1	$F_1(x,\tau)$	$F_1(x,\tau)$	NC-FD → NC-FD
	Ω_2	Ω_1	$F_2(x,\tau)$	$F_1(x,\tau)$	NC-S → NC-FD
	Ω_3	Ω_1	$F_3(x,\tau)$	$F_1(x,\tau)$	NC-BD → NC-FD
L_2	Ω_1	Ω_2	$F_1(x,\tau)$	$F_2(x,\tau)$	NC-FD → NC-S
	Ω_2	Ω_2	$F_2(x,\tau)$	$F_2(x,\tau)$	NC-S → NC-S
	Ω_3	Ω_2	$F_3(x,\tau)$	$F_2(x,\tau)$	NC-BD → NC-S
	Ω_1	Ω_3	$F_1(x,\tau)$	$F_3(x,\tau)$	NC-FD → NC-BD
	Ω_2	Ω_3	$F_2(x,\tau)$	$F_3(x,\tau)$	NC-S → NC-BD
	Ω_3	Ω_3	$F_3(x,\tau)$	$F_3(x,\tau)$	NC-BD → NC-BD
L_3	Ω_4	Ω_4	$F_4(x,\tau)$	$F_4(x,\tau)$	C-FD → C-FD
	Ω_5	Ω_4	$F_5(x,\tau)$	$F_4(x,\tau)$	C-S → C-FD
	Ω_6	Ω_4	$F_6(x,\tau)$	$F_4(x,\tau)$	C-BD → C-FD
	Ω_4	Ω_5	$F_4(x,\tau)$	$F_5(x,\tau)$	C-FD → C-S
	Ω_5	Ω_5	$F_5(x,\tau)$	$F_5(x,\tau)$	C-S → C-S
	Ω_6	Ω_5	$F_6(x,\tau)$	$F_5(x,\tau)$	C-BD → C-S
L_4	Ω_4	Ω_4	$F_4(x,\tau)$	$F_4(x,\tau)$	C-FD → C-FD
	Ω_5	Ω_4	$F_5(x,\tau)$	$F_4(x,\tau)$	C-S → C-FD
	Ω_6	Ω_4	$F_6(x,\tau)$	$F_4(x,\tau)$	C-BD → C-FD
L_5	Ω_3	Ω_4	$F_3(x,\tau)$	$F_4(x,\tau)$	NC-BD → C-FD
L_6	Ω_1	Ω_5	$F_1(x,\tau)$	$F_5(x,\tau)$	NC-FD → C-S
	Ω_2	Ω_5	$F_2(x,\tau)$	$F_5(x,\tau)$	NC-S → C-S
	Ω_3	Ω_5	$F_3(x,\tau)$	$F_5(x,\tau)$	NC-BD → C-S
L_7	Ω_4	Ω_2	$F_4(x,\tau)$	$F_2(x,\tau)$	C-FD → NC-S
	Ω_5	Ω_2	$F_5(x,\tau)$	$F_2(x,\tau)$	C-S → NC-S
	Ω_6	Ω_2	$F_6(x,\tau)$	$F_2(x,\tau)$	C-BD → NC-S
L_8	Ω_4	Ω_3	$F_4(x,\tau)$	$F_3(x,\tau)$	C-FD → NC-BD

summary, all possible 3D local mappings for the capsule system are given in Table 3.

4. Numerical studies

Numerical studies by varying the amplitude of excitation are given in this section to show how the proposed 3D map can be used to describe and explain the dynamics of the capsule system with a focus on its switching mechanisms on the non-smooth boundaries. The overall influence of α on the dynamics of the capsule system is presented in Fig. 6, calculated for $\omega = 0.8$, $\delta = 0.02$, $\zeta = 0.05$, $\beta = 1.5$ and $\gamma = 3.3$. As α increases from 0 to 2, grazing, adding–sliding, boundary-intersection crossing, crossing–sliding, switching–sliding and grazing–sliding bifurcations can be observed.

Based on various bifurcations encountered when the amplitude of excitation increases, dynamics of the capsule system is considered from the following regimes. For each typical trajectory, the displacements of the inner mass and the capsule are shown in Fig. 7, together with its phase portrait, to explain how the orbit switches from one non-smooth boundary to another. The dynamics of the capsule system for each regime is summarised as follows.

- $\alpha \in (0, 0.0074]$: As shown in Fig. 7(a), the global mapping of the capsule system can be represented by an identity mapping, $P = Id_{\Sigma_2,F_2,\Sigma_2}$, which is dominated by $F_2(x,\tau)$, and the capsule is kept stationary without any impact. For $\alpha = 0.0074$, a grazing bifurcation is encountered, and the system trajectory passes L_9 tangentially. Further increase of α will lead to the occurrence of impacts.
- $\alpha \in (0.0074, 0.3687]$: As shown in Fig. 7(b), the global mapping can be written as $P = P_{\Sigma_5,F_2,\Sigma_2} \circ P_{\Sigma_2,F_5,\Sigma_5}$. The capsule is kept stationary with one impact per period of excitation.

Table 3
All 3D local mappings for the capsule system.

Mapping	Operation	Vector	Mapping	Operation	Vector
$P_{\Sigma_2,F_1,\Sigma_1}$	$\Sigma_2 \xleftarrow{F_1} \Sigma_1$	NC-FD	$P_{\Sigma_2,F_1,\Sigma_8}$	$\Sigma_2 \xleftarrow{F_1} \Sigma_8$	NC-FD
$P_{\Sigma_3,F_1,\Sigma_1}$	$\Sigma_3 \xleftarrow{F_1} \Sigma_1$	NC-FD	$P_{\Sigma_3,F_1,\Sigma_8}$	$\Sigma_3 \xleftarrow{F_1} \Sigma_8$	NC-FD
$P_{\Sigma_5,F_1,\Sigma_1}$	$\Sigma_5 \xleftarrow{F_1} \Sigma_1$	NC-FD	$P_{\Sigma_5,F_1,\Sigma_8}$	$\Sigma_5 \xleftarrow{F_1} \Sigma_8$	NC-FD
$P_{\Sigma_7,F_1,\Sigma_1}$	$\Sigma_7 \xleftarrow{F_1} \Sigma_1$	NC-FD	$P_{\Sigma_7,F_1,\Sigma_8}$	$\Sigma_7 \xleftarrow{F_1} \Sigma_8$	NC-FD
$P_{\Sigma_1,F_2,\Sigma_2}$	$\Sigma_1 \xleftarrow{F_2} \Sigma_2$	NC-S	$P_{\Sigma_2,F_5,\Sigma_5}$	$\Sigma_2 \xleftarrow{F_5} \Sigma_5$	C-S
$P_{\Sigma_3,F_2,\Sigma_2}$	$\Sigma_3 \xleftarrow{F_2} \Sigma_2$	NC-S	$P_{\Sigma_4,F_5,\Sigma_5}$	$\Sigma_4 \xleftarrow{F_5} \Sigma_5$	C-S
$P_{\Sigma_5,F_2,\Sigma_2}$	$\Sigma_5 \xleftarrow{F_2} \Sigma_2$	NC-S	$P_{\Sigma_6,F_5,\Sigma_5}$	$\Sigma_6 \xleftarrow{F_5} \Sigma_5$	C-S
$P_{\Sigma_1,F_3,\Sigma_3}$	$\Sigma_1 \xleftarrow{F_3} \Sigma_3$	NC-BD	$P_{\Sigma_1,F_3,\Sigma_{10}}$	$\Sigma_1 \xleftarrow{F_3} \Sigma_{10}$	NC-BD
$P_{\Sigma_2,F_3,\Sigma_3}$	$\Sigma_2 \xleftarrow{F_3} \Sigma_3$	NC-BD	$P_{\Sigma_2,F_3,\Sigma_{10}}$	$\Sigma_2 \xleftarrow{F_3} \Sigma_{10}$	NC-BD
$P_{\Sigma_4,F_3,\Sigma_3}$	$\Sigma_4 \xleftarrow{F_3} \Sigma_3$	NC-BD	$P_{\Sigma_4,F_3,\Sigma_{10}}$	$\Sigma_4 \xleftarrow{F_3} \Sigma_{10}$	NC-BD
$P_{\Sigma_5,F_3,\Sigma_3}$	$\Sigma_5 \xleftarrow{F_3} \Sigma_3$	NC-BD	$P_{\Sigma_5,F_3,\Sigma_{10}}$	$\Sigma_5 \xleftarrow{F_3} \Sigma_{10}$	NC-BD
$P_{\Sigma_9,F_3,\Sigma_3}$	$\Sigma_9 \xleftarrow{F_3} \Sigma_3$	NC-BD	$P_{\Sigma_9,F_3,\Sigma_{10}}$	$\Sigma_9 \xleftarrow{F_3} \Sigma_{10}$	NC-BD
$P_{\Sigma_2,F_4,\Sigma_4}$	$\Sigma_2 \xleftarrow{F_4} \Sigma_4$	C-FD	$P_{\Sigma_2,F_4,\Sigma_7}$	$\Sigma_2 \xleftarrow{F_4} \Sigma_7$	C-FD
$P_{\Sigma_3,F_4,\Sigma_4}$	$\Sigma_3 \xleftarrow{F_4} \Sigma_4$	C-FD	$P_{\Sigma_3,F_4,\Sigma_7}$	$\Sigma_3 \xleftarrow{F_4} \Sigma_7$	C-FD
$P_{\Sigma_5,F_4,\Sigma_4}$	$\Sigma_5 \xleftarrow{F_4} \Sigma_4$	C-FD	$P_{\Sigma_5,F_4,\Sigma_7}$	$\Sigma_5 \xleftarrow{F_4} \Sigma_7$	C-FD
$P_{\Sigma_6,F_4,\Sigma_4}$	$\Sigma_6 \xleftarrow{F_4} \Sigma_4$	C-FD	$P_{\Sigma_6,F_4,\Sigma_7}$	$\Sigma_6 \xleftarrow{F_4} \Sigma_7$	C-FD
$P_{\Sigma_8,F_4,\Sigma_4}$	$\Sigma_8 \xleftarrow{F_4} \Sigma_4$	C-FD	$P_{\Sigma_8,F_4,\Sigma_7}$	$\Sigma_8 \xleftarrow{F_4} \Sigma_7$	C-FD
$P_{\Sigma_2,F_6,\Sigma_6}$	$\Sigma_2 \xleftarrow{F_6} \Sigma_6$	C-BD	$P_{\Sigma_2,F_6,\Sigma_9}$	$\Sigma_2 \xleftarrow{F_6} \Sigma_9$	C-BD
$P_{\Sigma_4,F_6,\Sigma_6}$	$\Sigma_4 \xleftarrow{F_6} \Sigma_6$	C-BD	$P_{\Sigma_4,F_6,\Sigma_9}$	$\Sigma_4 \xleftarrow{F_6} \Sigma_9$	C-BD
$P_{\Sigma_5,F_6,\Sigma_6}$	$\Sigma_5 \xleftarrow{F_6} \Sigma_6$	C-BD	$P_{\Sigma_5,F_6,\Sigma_9}$	$\Sigma_5 \xleftarrow{F_6} \Sigma_9$	C-BD
$P_{\Sigma_{10},F_6,\Sigma_6}$	$\Sigma_{10} \xleftarrow{F_6} \Sigma_6$	C-BD	$P_{\Sigma_{10},F_6,\Sigma_9}$	$\Sigma_{10} \xleftarrow{F_6} \Sigma_9$	C-BD

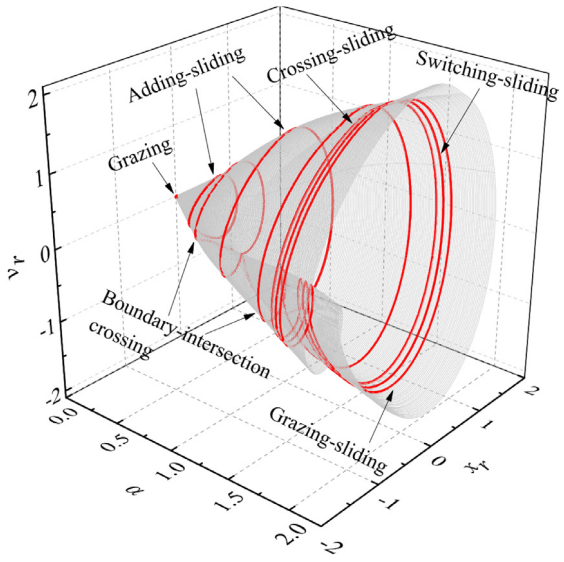

Fig. 6. Evolution of phase trajectories of the capsule system in the state space (x_r, v_r) under variation of the amplitude of excitation $\alpha \in [0, 2]$. As α increases, grazing, adding–sliding, boundary-intersection crossing, crossing–sliding, switching–sliding and grazing–sliding bifurcations are observed. Simulation conditions are $\omega = 0.8$, $\delta = 0.02$, $\zeta = 0.05$, $\beta = 1.5$, and $\gamma = 3.3$ by using initial state $(x_r, v_r, v_c) = (0, 0, 0)$. (For interpretation of the references to colour in this figure legend, the reader is referred to the web version of this article.)

When $\alpha = 0.3687$, as shown in Fig. 6(c), an adding–sliding bifurcation occurs, and the trajectory (the black segment) passes $L_3^{(2)}$ tangentially. As α further increases, the capsule will move forward.

- $\alpha \in (0.3687, 0.5245)$: As shown in Fig. 7(d), the global mapping of the capsule system can be represented by $P = P_{\Sigma_5,F_2,\Sigma_2} \circ P_{\Sigma_2,F_5,\Sigma_5} \circ P_{\Sigma_5,F_4,\Sigma_4} \circ P_{\Sigma_4,F_5,\Sigma_5}$, where the local mapping $P_{\Sigma_5,F_4,\Sigma_4}$ indicates a forward drift of the capsule.
- $\alpha = 0.5245$: A boundary-intersection crossing bifurcation occurs as shown in Fig. 7(e), when the trajectory (the green segment) hits and passes through L_7 from Σ_4 to Σ_2 directly. Therefore, the global mapping can be represented as $P = P_{\Sigma_5,F_2,\Sigma_2} \circ P_{\Sigma_2,F_4,\Sigma_4} \circ P_{\Sigma_4,F_5,\Sigma_5}$. Further increase of α will make the trajectory leave the impact boundary through S_8. The 3D trajectories for the boundary-intersection crossing bifurcation around $\alpha = 0.5245$ are shown in Fig. 8(a) and (b).
- $\alpha \in (0.5245, 0.939]$: As shown in Fig. 7(f), the global mapping for this regime can be written as $P = P_{\Sigma_5,F_2,\Sigma_2} \circ P_{\Sigma_2,F_1,\Sigma_8} \circ P_{\Sigma_8,F_4,\Sigma_4} \circ P_{\Sigma_4,F_5,\Sigma_5}$. For the segments of $F_4(x, \tau)$ and $F_1(x, \tau)$, the capsule moves forward without and with impact, respectively. For $\alpha = 0.939$ as shown in Fig. 7(g), an adding–sliding bifurcation is encountered, and the trajectory (the red segment) passes L_2 tangentially. As α increases further, backward motion of the capsule can be observed. A detailed adding–sliding bifurcation around $\alpha = 0.939$ can be found in Fig. 9(a).
- $\alpha \in (0.939, 1.443)$: The global mapping for this regime can be represented as $P = P_{\Sigma_5,F_2,\Sigma_2} \circ P_{\Sigma_2,F_3,\Sigma_3} \circ P_{\Sigma_3,F_2,\Sigma_2} \circ P_{\Sigma_2,F_1,\Sigma_8} \circ P_{\Sigma_8,F_4,\Sigma_4} \circ P_{\Sigma_4,F_5,\Sigma_5}$. As can be seen from the trajectory shown in Fig. 7(h), the magenta segment for backward drift dominated by $F_3(x, \tau)$ is inserted between the red segments dominated by $F_2(x, \tau)$.
- $\alpha = 1.443$: A boundary-intersection crossing bifurcation occurs at $\alpha = 1.443$, when the trajectory (the magenta segment) hits L_6 as shown in Fig. 7(i), at where $P_{\Sigma_5,F_3,\Sigma_3}$ maps the trajectory from Σ_3 into Σ_5 directly. A detailed 3D trajectory for this bifurcation around $\alpha = 1.443$ can be found from Fig. 8(c) and (d). The global mapping can be given as

Please cite this article as: B. Guo and Y. Liu, Three-dimensional map for a piecewise-linear capsule system with bidirectional drifts, Physica D (2019), https://doi.org/10.1016/j.physd.2019.04.008.

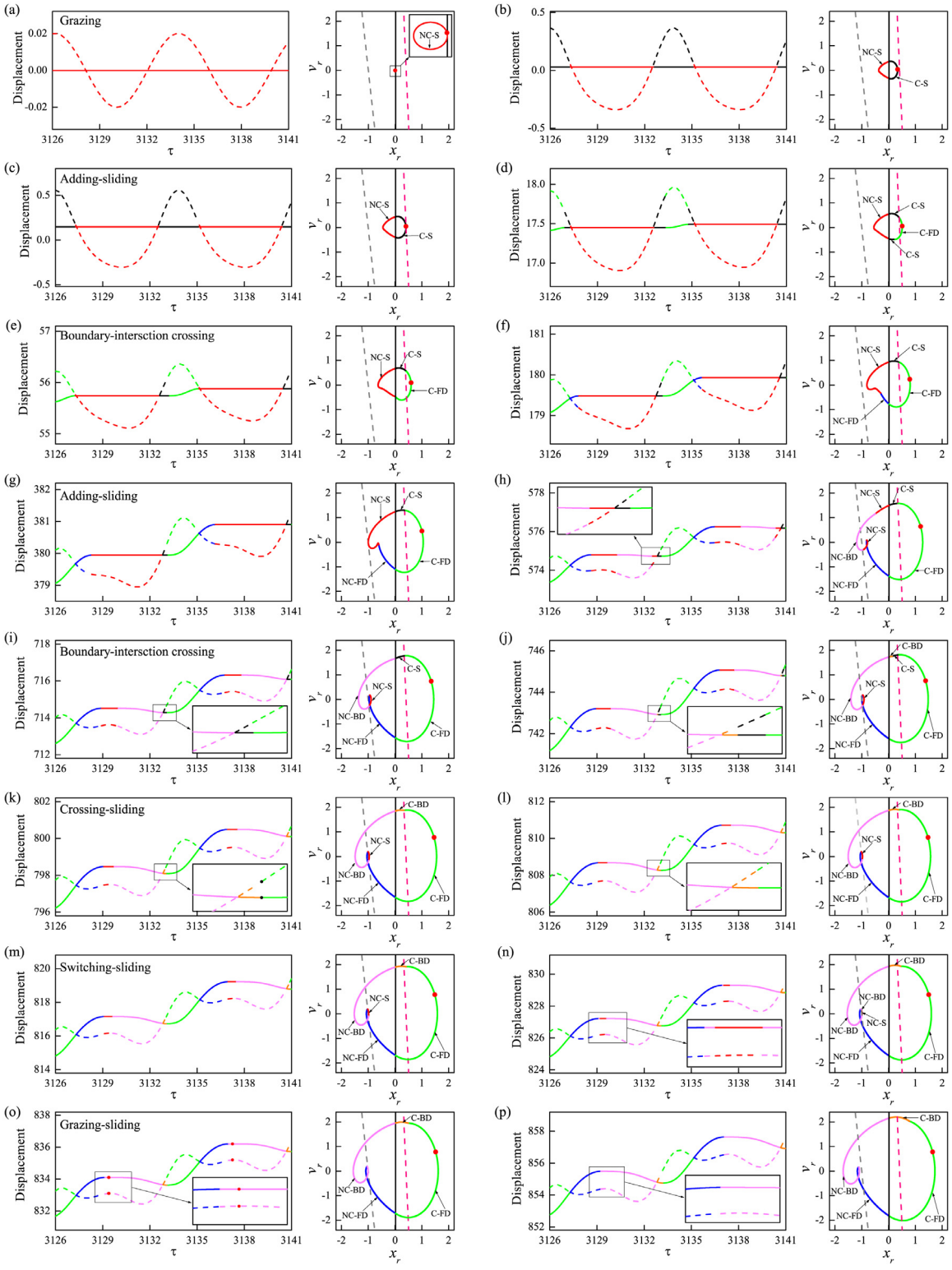

Fig. 7. Displacements of the inner mass (dashed lines) and the capsule (solid lines), and phase portraits of the capsule system for varied amplitude of excitation, α, calculated for $\omega = 0.8$, $\delta = 0.02$, $\zeta = 0.05$, $\beta = 1.5$, and $\gamma = 3.3$. The amplitude of excitation for (a)–(p) are $\alpha = 0.0074, 0.3, 0.3687, 0.4, 0.5245, 0.7, 0.939, 1.2, 1.443, 1.5, 1.6148, 1.64, 1.661, 1.69, 1.7126, 1.9$, respectively. The blue, red, magenta, green, black, and orange lines represent the trajectory segments dominated by $F_{n=1,2,\ldots,6}$, respectively. On the phase portraits, The grey dashed, black solid and red dashed lines represent the non-smooth boundaries, L_2, $L_6 \cup L_7$ and L_3, respectively. (For interpretation of the references to colour in this figure legend, the reader is referred to the web version of this article.)

$P = P_{\Sigma_5,F_3,\Sigma_3} \circ P_{\Sigma_3,F_2,\Sigma_2} \circ P_{\Sigma_2,F_1,\Sigma_8} \circ P_{\Sigma_8,F_4,\Sigma_4} \circ P_{\Sigma_4,F_5,\Sigma_5}$. As the amplitude of excitation increases, the trajectory will enter the impact boundary through S_9.

- $\alpha \in (1.443, 1.6148]$: The global mapping for this regime can be represented by $P = P_{\Sigma_5,F_6,\Sigma_9} \circ P_{\Sigma_9,F_3,\Sigma_3} \circ P_{\Sigma_3,F_2,\Sigma_2} \circ P_{\Sigma_2,F_1,\Sigma_8} \circ P_{\Sigma_8,F_4,\Sigma_4} \circ P_{\Sigma_4,F_5,\Sigma_5}$. As can be seen from Fig. 7(j),

Please cite this article as: B. Guo and Y. Liu, Three-dimensional map for a piecewise-linear capsule system with bidirectional drifts, Physica D (2019), https://doi.org/10.1016/j.physd.2019.04.008.

the trajectory enters the impact boundary through S_9, and the orange segment of $F_6(x, \tau)$ is inserted. For $\alpha = 1.6148$ as shown in Fig. 7(k), a crossing–sliding bifurcation is encountered, and the trajectory approaches to S_4 after passing L_3 (There is only one point on L_3, represented by the black dot in Fig. 7(k)). Further increase of α will drive the trajectory from Σ_9 to Σ_4, and consequently, the sticking segment governed by $F_5(x, \tau)$ will vanish. Detailed 3D trajectories around $\alpha = 1.6148$ are shown in Fig. 9(b).

- $\alpha \in (1.6148, 1.661]$: As shown in Fig. 7(l), the global mapping for this regime is given as $P = P_{\Sigma_9,F_3,\Sigma_3} \circ P_{\Sigma_3,F_2,\Sigma_2} \circ P_{\Sigma_2,F_1,\Sigma_8} \circ P_{\Sigma_8,F_4,\Sigma_4} \circ P_{\Sigma_4,F_6,\Sigma_9}$. For $\alpha = 1.661$ shown in Fig. 7(m), a switching–sliding bifurcation occurs, and the trajectory (the blue segment) approaches to S_2 after passing L_2. If α is further increased, the trajectory will be driven from S_8 to S_3 rather than S_2. For this switching–sliding bifurcation, the detailed 3D trajectories around $\alpha = 1.661$ are shown in Fig. 9(c).
- $\alpha \in (1.661, 1.7126]$: As illustrated in Fig. 7(n), the global mapping for this regime can be represented using $P = P_{\Sigma_9,F_3,\Sigma_3} \circ P_{\Sigma_3,F_2,\Sigma_2} \circ P_{\Sigma_2,F_3,\Sigma_3} \circ P_{\Sigma_3,F_1,\Sigma_8} \circ P_{\Sigma_8,F_4,\Sigma_4} \circ P_{\Sigma_4,F_6,\Sigma_9}$. When $\alpha = 1.7126$ as shown in Fig. 6(o), a grazing–sliding bifurcation is encountered, and the trajectory passes L_2 tangentially (There is only one point on L_2, represented by the red dot in Fig. 7(o)). Further increase in α will lead to the vanishing of sticking segment governed by $F_2(x, \tau)$. A detailed presentation of this grazing–sliding bifurcation around $\alpha = 1.7126$ is shown in Fig. 9(d).
- $\alpha \in (1.7126, 2]$: As shown in Fig. 7(p), the global mapping for this regime can be represented using $P = P_{\Sigma_9,F_3,\Sigma_3} \circ P_{\Sigma_3,F_1,\Sigma_8} \circ P_{\Sigma_8,F_4,\Sigma_4} \circ P_{\Sigma_4,F_6,\Sigma_9}$, and there is no sticking segment found in this mapping.

To depict the boundary-intersection crossing bifurcations around $\alpha = 0.5245$ and $\alpha = 1.443$ in detail, system trajectories are plotted with the non-smooth boundary lines in 3D space in Fig. 8. As shown in Fig. 8(a) and (b), the local mapping $P_{\Sigma_2,F_4,\Sigma_4}$ (the green segment) hits L_7 at $\alpha = 0.5245$, which is the intersection line of S_5 and S_8. A slight increase ($\alpha = 0.6$) or decrease ($\alpha = 0.4$) in α will lead the trajectories to reach S_8 or S_5, respectively. As a consequence, the local and global mappings are changed, and boundary-intersection crossing bifurcation occurs around $\alpha = 0.5245$. As shown in Fig. 8(c)–(d), a boundary-intersection crossing bifurcation happens around $\alpha = 1.443$ and the magenta segment of $P_{\Sigma_5,F_3,\Sigma_3}$ hits L_6, which is the intersection line of S_2 and S_9. A slight increase ($\alpha = 1.5$) or decrease ($\alpha = 1.4$) in α will lead the trajectories to reach S_9 or S_2, respectively. Therefore, boundary-intersection crossing bifurcations can be detected by using the 3D local mappings, among which $P_{\Sigma_2,F_4,\Sigma_4}$ and $P_{\Sigma_5,F_3,\Sigma_3}$ indicate the occurrence of boundary-intersection crossing bifurcations on L_7 and L_6, respectively.

The non-smoothness in dry friction induces stick–slip motion for the capsule system, where sliding regions are bounded by $L_{j=1,2,3,4}$. When orbits hit on these lines, adding–sliding, crossing–sliding, switching–sliding and grazing–sliding bifurcations may occur. As shown in Fig. 9, the cases for $\alpha = 0.939$, 1.6148, 1.661, and 1.7126 are taken as examples to study each type of sliding bifurcations, which are described as follows.

- **Adding–sliding bifurcation:** As shown in Fig. 9(a), an adding–sliding bifurcation occurs around $\alpha = 0.939$. The sliding segment $P_{\Sigma_5,F_2,\Sigma_2}$ is tangent to the boundary line $L_2^{(2)}$, and any infinitely small increase in α ($\alpha = 1.2$) will lead to a backward motion segment represented by $F_3(x, \tau)$. Another adding–sliding bifurcation happens on $L_3^{(2)}$ for $\alpha = 0.3687$, as shown in Fig. 6(d), and thereafter, a forward motion dominated by $F_4(x, \tau)$ is added. As discussed in Section 3.3, the adding–sliding bifurcation can only happen when the trajectory passes $L_2^{(2)}$ or $L_3^{(2)}$ tangentially.
- **Crossing–sliding bifurcation:** As shown in Fig. 9(b), a crossing–sliding bifurcation occurs around $\alpha = 1.6148$, and the local mapping $P_{\Sigma_5,F_6,\Sigma_9}$ crosses the boundary via $L_3^{(3)}$. An infinitely small perturbation in α will change the way that the trajectory passes the non-smooth boundary of $P_1(x) = 0$. If the trajectory passes the $P_1(x) = 0$ plane through S_5, sliding segments dominated by $F_5(x, \tau)$ may exist in global mappings. If an orbit reaches S_4 directly, sliding segments dominated by $F_5(x, \tau)$ will disappear.
- **Switching–sliding bifurcation:** As shown in Fig. 9(c), a switching–sliding bifurcation occurs around $\alpha = 1.661$, and the local mapping $P_{\Sigma_2,F_1,\Sigma_8}$ hits the boundary line $L_2^{(2)}$. An infinitely small perturbation in α will change the way how the trajectory approaches into the sliding region of S_2. For $\alpha < 1.661$, e.g., $\alpha = 1.64$, the segment $P_{\Sigma_2,F_1,\Sigma_8}$ approaches to S_2 directly. For $\alpha > 1.661$, e.g., $\alpha = 1.69$, the segment $P_{\Sigma_3,F_1,\Sigma_8}$ approaches to S_3 first and then reaches S_2.
- **Grazing–sliding bifurcation:** As shown in Fig. 9(d), a grazing–sliding bifurcation occurs around $\alpha = 1.7126$, and the local mapping $P_{\Sigma_2,F_3,\Sigma_3}$ grazes the boundary line $L_2^{(2)}$. The segment in Σ_2 degenerates to the tangent point on $L_2^{(2)}$ and approaches to S_3 immediately. Any infinitely small increase in α will make the sliding segments dominated by $F_2(x, \tau)$ vanish.

5. Conclusions

This paper studied a 3D map for the piecewise-linear capsule system with bidirectional drifts. The purpose of this study is to provide a general analytical tool for studying its global and local dynamics associated with the non-smooth boundaries induced by dry friction and impact. Based on the analysis of the vector field in the vicinities of the non-smooth boundary surfaces and lines, the switching mechanisms on the non-smooth planes were determined, and all possible local mappings were obtained. By using the switching mechanisms, it can reveal the relationship between system trajectory and the non-smooth boundaries, and this could be used to explain the occurrence of boundary-intersection crossing and sliding bifurcations in the capsule system. Furthermore, the global map of the capsule system can also be obtained by constructing relevant local mappings according to the switching mechanisms studied in this paper.

By investigating various amplitudes of the external excitation, it is found that for a small amplitude ($\alpha \leq 0.3687$), the capsule is kept stationary and the system orbits are constrained within the sliding regions. Adding–sliding bifurcation may occur around $\alpha = 0.3687$ and $\alpha = 0.939$ when system orbits are tangent to the sliding boundary lines $L_3^{(2)}$ and $L_2^{(2)}$, indicating the occurrence of forward and backward motions, respectively. Crossing–sliding, switching–sliding, and grazing–sliding bifurcations were observed when system orbits hit the sliding boundary lines $L_{j=1,2,3,4}$, determining the disappearance of sliding segments. Additionally, boundary-intersection crossing bifurcations occur when system orbits hit the intersection lines $L_{j=5,6,7,8}$, which can be detected directly by using local mappings.

Our numerical case studies demonstrate the validity of the proposed switching mechanisms on the non-smooth boundary lines and surfaces. The results illustrate that the proposed 3D global and local mappings can be used as an analytical tool to explain the occurrence of bifurcations and to investigate local and global properties of the capsule system. Future work on the 3D map will focus on deriving the analytical solution of the capsule system in order to optimise its trajectory for enhancing the rate of progression and power efficiency.

Please cite this article as: B. Guo and Y. Liu, Three-dimensional map for a piecewise-linear capsule system with bidirectional drifts, Physica D (2019), https://doi.org/10.1016/j.physd.2019.04.008.

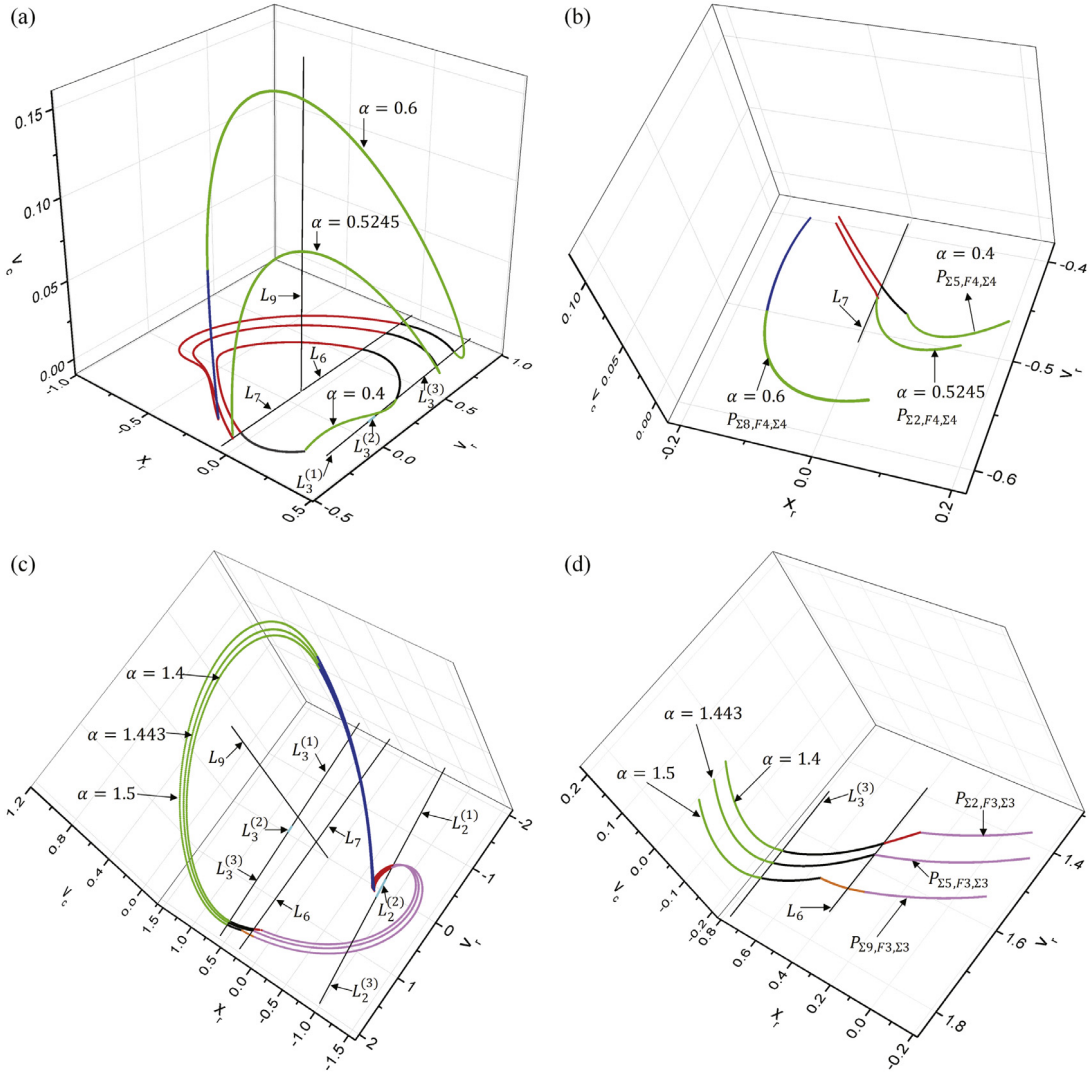

Fig. 8. (a)–(b) A boundary-intersection crossing bifurcation occurs around $\alpha = 0.5245$ and its trajectory passes L_7. The green segment $P_{\Sigma_2,F_4,\Sigma_4}$ maps the trajectory from $L_3^{(3)}$ to L_7 directly. For a slightly smaller α ($\alpha = 0.4$), the trajectory will go out from $L_3^{(3)}$ and enter S_5. For a slightly larger α ($\alpha = 0.6$), the segment will go out from $L_3^{(3)}$ and reach S_8. (c)–(d) A boundary-intersection crossing bifurcation occurs around $\alpha = 1.443$ when the trajectory passes L_6. The magenta segment $P_{\Sigma_5,F_3,\Sigma_3}$ maps the trajectory from $L_2^{(1)}$ to L_6 directly. For a slightly smaller α ($\alpha = 1.4$), the trajectory will go out from $L_2^{(1)}$ and enter S_2. For a slightly larger α ($\alpha = 1.5$), the segment will go out from $L_2^{(1)}$ and reach S_9. The blue, red, magenta, green, black, and orange lines represent the trajectory segments dominated by $F_{n=1,2,\ldots,6}$, respectively. (For interpretation of the references to colour in this figure legend, the reader is referred to the web version of this article.)

Acknowledgements

This work has been supported by EPSRC, UK under Grant No. EP/P023983/1, and was partially supported by the National Natural Science Foundation of China under Grant No. 11672257. The authors thank Professor Joseph Páez Chávez for useful discussion on constructing the 3D map.

Appendix A

The switching mechanism on L_1 depends on the sign of $\left\langle \nabla P_3^+(x), F_2(x,\tau)\right\rangle\big|_{x=x_1}$, expressed in Eq. (22). Here we assume that the sign is positive for any point x_1 on L_1 at any time τ, given as

$$\left\langle \nabla P_3^+(x), F_2(x,\tau)\right\rangle\big|_{x=x_1} = v_r - 2\zeta f_b + 2\zeta\alpha\cos(\omega\tau) > 0. \tag{A.1}$$

Eq. (A.1) can be modified as

$$\alpha\cos(\omega\tau) > f_b - \frac{v_r}{2\zeta}. \tag{A.2}$$

As x_1 is a point on the line L_1, we have $v_r > \frac{f_b-\delta}{2\zeta}$. To make Eq. (A.1) valid for any point x_1 on L_1 at any time τ, one sufficient condition is

$$\min(\alpha\cos(\omega\tau)) > \max(f_b - \frac{v_r}{2\zeta}). \tag{A.3}$$

Therefore, we have

$$-\alpha > f_b - \frac{f_b-\delta}{4\zeta^2}. \tag{A.4}$$

When the amplitude of the driven force $\alpha \in (0, \frac{f_b-\delta}{4\zeta^2} - f_b)$, the sign of $\left\langle \nabla P_3^+(x), F_2(x,\tau)\right\rangle\big|_{x=x_1}$ is positive for any point x_1 on L_1 at any time τ, and hence the switching mechanism on L_1 is uni-directional, pointing from S_2 to S_1.

Based on the same principle, when the amplitude of the forcing, $\alpha \in (0, \frac{(1+\beta)(f_b+\delta)}{4\zeta^2} - f_b)$, the sign of $\left\langle \nabla P_4^-(x), F_5(x,\tau)\right\rangle\big|_{x=x_4}$ is positive for any point x_4 on L_4 at any time τ, and hence, the switching mechanism on L_4 is uni-directional, pointing from S_5

Please cite this article as: B. Guo and Y. Liu, Three-dimensional map for a piecewise-linear capsule system with bidirectional drifts, Physica D (2019), https://doi.org/10.1016/j.physd.2019.04.008.

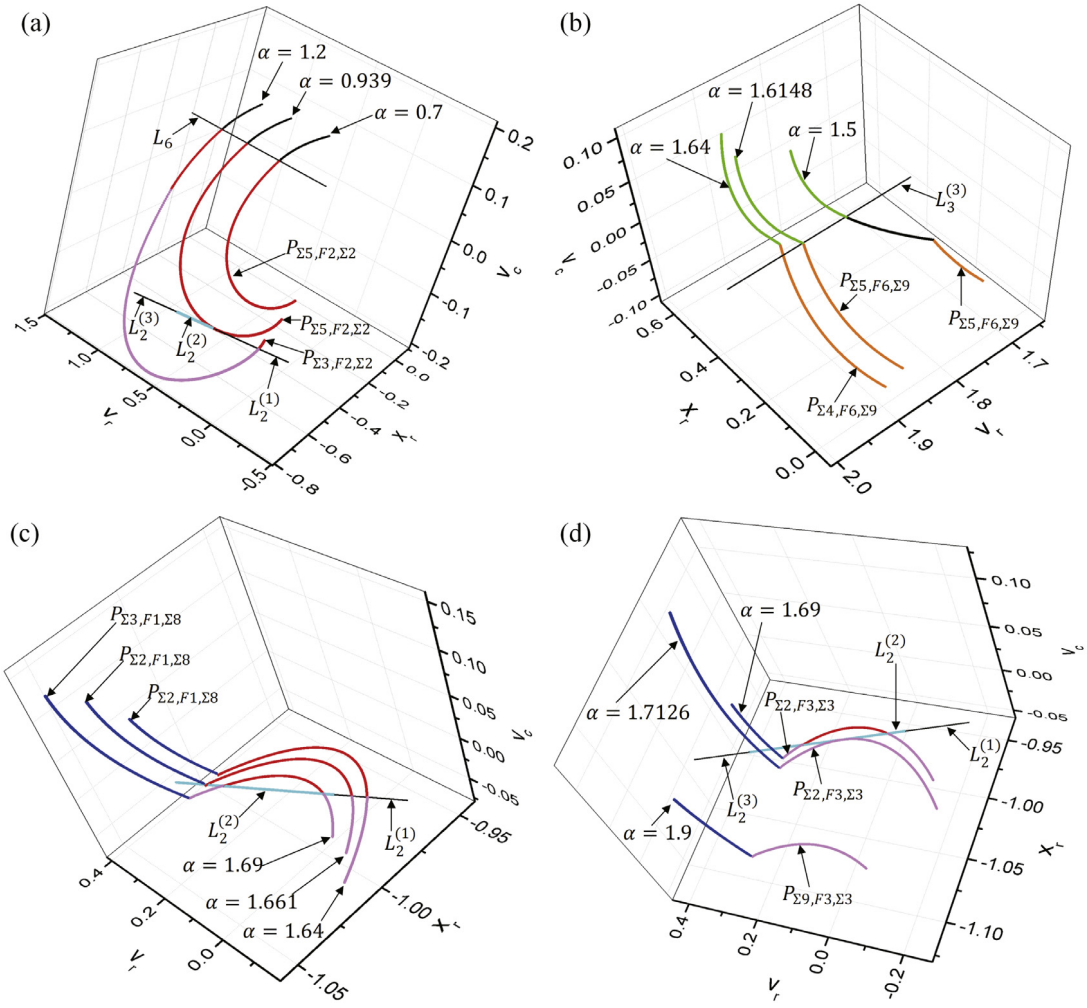

Fig. 9. (a) An adding–sliding bifurcation occurs around $\alpha = 0.939$, where the red segment $P_{\Sigma_5,F_2,\Sigma_2}$ is tangent to $L_2^{(2)}$. A slight increase in α will add a backward motion segment. For instance, when $\alpha = 1.2$, it changes the local mapping to $P_{\Sigma_3,F_2,\Sigma_2}$, and consequently, a backward motion $P_{\Sigma_2,F_3,\Sigma_3}$ (the magenta segment) is added. (b) A crossing–sliding bifurcation occurs around $\alpha = 1.6148$, where the orange segment $P_{\Sigma_5,F_6,\Sigma_9}$ hits $L_3^{(3)}$. A smaller α ($\alpha = 1.5$) indicates the existence of sliding motion (the black segment) represented by $F_5(x,\tau)$, whilst a larger α ($\alpha = 1.64$) indicates the vanishing of the sliding segment (the black one). (c) A switching–sliding bifurcation occurs around $\alpha = 1.661$, where the blue segment $P_{\Sigma_2,F_1,\Sigma_8}$ hits $L_2^{(2)}$ and enters S_2. A slight increase in α, e.g., $\alpha = 1.69$, will change the trajectory mapping into S_3 and then into S_2. For a smaller α, e.g., $\alpha = 1.64$, the segment $P_{\Sigma_2,F_1,\Sigma_8}$ approaches to S_2 directly. (d) A grazing–sliding bifurcation occurs around $\alpha = 1.7126$, where the magenta segment $P_{\Sigma_2,F_3,\Sigma_3}$ grazes $L_2^{(2)}$. A smaller α, e.g., $\alpha = 1.69$, indicates the existence of sliding segment dominated by $F_2(x,\tau)$, whilst a larger α, e.g., $\alpha = 1.9$, indicates the disappearance of the sliding motion described by $F_2(x,\tau)$. The blue, red, magenta, green, black, and orange lines represent the trajectory segments dominated by $F_{n=1,2,\ldots,6}$, respectively. (For interpretation of the references to colour in this figure legend, the reader is referred to the web version of this article.)

to S_6. Therefore, $\alpha \in (0, \frac{f_b-\delta}{4\zeta^2} - f_b) \cap (0, \frac{(1+\beta)(f_b+\delta)}{4\zeta^2} - f_b)$ ensures that the switching directions on L_1 and L_4 are unitary.

Appendix B

The switching mechanism on the line L_2 depends on the sign of $\left\langle \nabla P_3^-(x), F_2(x,\tau)\right\rangle\big|_{x=x_2}$. To determine its sign, here we discuss the existence condition of the solution for $\left\langle \nabla P_3^-(x), F_2(x,\tau)\right\rangle\big|_{x=x_2} = 0$. Here, we assume there exists v_r and τ, satisfying

$$\left\langle \nabla P_3^-(x), F_2(x,\tau)\right\rangle\big|_{x=x_2} = -v_r + 2\zeta f_b + 2\zeta\alpha\cos(\omega\tau) = 0. \quad \text{(B.1)}$$

Then we have

$$-2\zeta\alpha \le -v_r + 2\zeta f_b \le 2\zeta\alpha. \quad \text{(B.2)}$$

Therefore, for a given α, the necessary condition for the existence of the solution of Eq. (B.1) is $2\zeta f_b - 2\zeta\alpha \le v_r \le 2\zeta f_b + 2\zeta\alpha$. As a consequence, we will always have (i) for $v_r < 2\zeta f_b - 2\zeta\alpha$, $\left\langle \nabla P_3^-(x), F_2(x,\tau)\right\rangle\big|_{x=x_2} < 0$; (ii) for $2\zeta f_b - 2\zeta\alpha \le v_r \le 2\zeta f_b + 2\zeta\alpha$, the sign of $\left\langle \nabla P_3^-(x), F_2(x,\tau)\right\rangle\big|_{x=x_2}$ depends on the time τ significantly; and (iii) for $v_r > 2\zeta f_b + 2\zeta\alpha$, $\left\langle \nabla P_3^-(x), F_2(x,\tau)\right\rangle\big|_{x=x_2} > 0$. Therefore, the line L_2 can be divided into three segments for discussing its switching mechanism, namely $L_2^{(1)}$ for $v_r \in [-\frac{f_b-\delta}{2\zeta}, 2\zeta f_b - 2\zeta\alpha)$, $L_2^{(2)}$ for $v_r \in [2\zeta f_b - 2\zeta\alpha, 2\zeta f_b + 2\zeta\alpha]$, and $L_2^{(3)}$ for $v_r \in (2\zeta f_b + 2\zeta\alpha, +\infty)$.

Based on the same principle, for a given α, L_3 can be divided into three segments to discuss its switching mechanism, namely $L_3^{(1)}$ for $v_r \in (-\infty, \frac{2\zeta(f_b-\alpha)}{1+\beta})$, $L_3^{(2)}$ for $v_r \in [\frac{2\zeta(f_b-\alpha)}{1+\beta}, \frac{2\zeta(f_b+\alpha)}{1+\beta}]$, and $L_3^{(3)}$ for $v_r \in (\frac{2\zeta(f_b+\alpha)}{1+\beta}, \frac{f_b-\delta}{2\zeta}]$.

References

[1] J.M. Mirats Tur, W. Garthwaite, Robotic devices for water main in-pipe inspection: A survey, J. Field Robotics 27 (4) (2010) 491–508.

Please cite this article as: B. Guo and Y. Liu, Three-dimensional map for a piecewise-linear capsule system with bidirectional drifts, Physica D (2019), https://doi.org/10.1016/j.physd.2019.04.008.

[2] J. Aguilar, T. Zhang, F. Qian, M. Kingsbury, B. McInroe, N. Mazouchova, C. Li, R. Maladen, C. Gong, M. Travers, et al., A review on locomotion robophysics: the study of movement at the intersection of robotics, soft matter and dynamical systems, Rep. Progr. Phys. 79 (11) (2016) 110001.
[3] B.J. Nelson, I.K. Kaliakatsos, J.J. Abbott, Microrobots for minimally invasive medicine, Annu. Rev. Biomed. Eng. 12 (2010) 55–85.
[4] F.L. Chernous'ko, On the motion of a body containing a movable internal mass, Dokl. Phys. 50 (11) (2005) 593–597.
[5] P. Valdastri, R.J. Webster III, C. Quaglia, M. Quirini, A. Menciassi, P. Dario, A new mechanism for mesoscale legged locomotion in compliant tubular environments, IEEE Trans. Robot. 25 (5) (2009) 1047–1057.
[6] F.L. Chernous'ko, The optimal periodic motions of a two-mass system in a resistant medium, J. Appl. Math. Mech. 72 (2) (2008) 116–125.
[7] E. Pavlovskaia, M. Wiercigroch, C. Grebogi, Modeling of an impact system with a drift, Phys. Rev. E 64 (5) (2001) 056224.
[8] Y. Liu, M. Wiercigroch, E. Pavlovskaia, H. Yu, Modelling of a vibro-impact capsule system, Int. J. Mech. Sci. 66 (2013) 2–11.
[9] Y. Liu, E. Pavlovskaia, M. Wiercigroch, Z. Peng, Forward and backward motion control of a vibro-impact capsule system, Int. J. Non-Linear Mech. 70 (2015) 30–46.
[10] Y. Liu, E. Pavlovskaia, M. Wiercigroch, Experimental verification of the vibro-impact capsule model, Nonlinear Dynam. 83 (1–2) (2016) 1029–1041.
[11] Y. Liu, E. Pavlovskaia, D. Hendry, M. Wiercigroch, Vibro-impact responses of capsule system with various friction models, Int. J. Mech. Sci. 72 (2013) 39–54.
[12] S.W. Shaw, P.J. Holmes, A periodically forced piecewise linear oscillator, J. Sound Vib. 90 (1) (1983) 129–155.
[13] A.B. Nordmark, Non-periodic motion caused by grazing incidence in an impact oscillator, J. Sound Vib. 145 (2) (1991) 279–297.
[14] R.P.S. Han, A.C.J. Luo, W. Deng, Chaotic motion of a horizontal impact pair, J. Sound Vib. 181 (2) (1995) 231–250.
[15] A.C.J. Luo, R.P.S. Han, The dynamics of a bouncing ball with a sinusoidally vibrating table revisited, Nonlinear Dynam. 10 (1) (1996) 1–18.
[16] M. Di Bernardo, P. Kowalczyk, A. Nordmark, Bifurcations of dynamical systems with sliding: derivation of normal-form mappings, Physica D 170 (3–4) (2002) 175–205.
[17] E. Pavlovskaia, M. Wiercigroch, Low-dimensional maps for piecewise smooth oscillators, J. Sound Vib. 305 (4–5) (2007) 750–771.
[18] G.W. Luo, X.H. Lv, L. Ma, Periodic-impact motions and bifurcations in dynamics of a plastic impact oscillator with a frictional slider, Eur. J. Mech. A Solids 27 (2008) 1088–1107.
[19] J. Páez Chávez, Y. Liu, E. Pavlovskaia, M. Wiercigroch, Path-following analysis of the dynamical response of a piecewise-linear capsule system, Commun. Nonlinear Sci. Numer. Simul. 37 (2016) 102–114.

Please cite this article as: B. Guo and Y. Liu, Three-dimensional map for a piecewise-linear capsule system with bidirectional drifts, Physica D (2019), https://doi.org/10.1016/j.physd.2019.04.008.